ACS APPLIED MATERIALS & INTERFACES

Research Article

www.acsami.org

Charge Generation Measured for Fullerene–Helical Nanofilament Liquid Crystal Heterojunctions

Rebecca A. Callahan,[†,‡] David C. Coffey,[‡,§] Dong Chen,[∥] Noel A. Clark,[∥] Garry Rumbles,[†,‡] and David M. Walba*[,†,‡]

[†]Department of Chemistry and Biochemistry and the Liquid Crystal Materials Research Center, University of Colorado, Boulder, Colorado 80309, United States

[‡]Chemical and Materials Science Center, National Renewable Energy Laboratory, Golden, Colorado 80401, United States

[§]Department of Chemistry and Physics, Warren Wilson College, Swannanoa, North Carolina 28778, United States

[∥]Department of Physics and the Liquid Crystal Materials Research Center, University of Colorado, Boulder, Colorado 80309, United States

Supporting Information

ABSTRACT: The helical nanofilament (HNF) liquid crystal phase is an ordered architecture exhibiting interesting properties for charge transport. It is a small molecule self-assembly of stacked and twisted crystalline layers, which form alignable organic nanorods with half the surface area of the filaments consisting of aromatic sublayer edges. HNFs mixed with an electron acceptor generate an intriguing network for photoinduced electron transfer (PET). In this work, we characterize the structure of the HNF phase as processed into thin films with transmission electron microscopy (TEM) and X-ray diffraction (XRD). Additionally, we measure the flash-photolysis time-resolved microwave conductivity (TRMC) in samples where the HNF phase is fabricated into heterojunctions with the fullerenes C_{60} and $PC_{60}BM$, prototypical electron acceptors for organic photovoltaics. Two distinct microstructures of the thin films were identified and compared for PET. A near-unity charge generation yield is observed in a bilayer of HNFs with C_{60}. Moreover, the HNF phase is shown to be 10× better at charge generation than a lamellar structuring of the same components. Thus, the HNF phase is shown to be a good charge-generation interface.

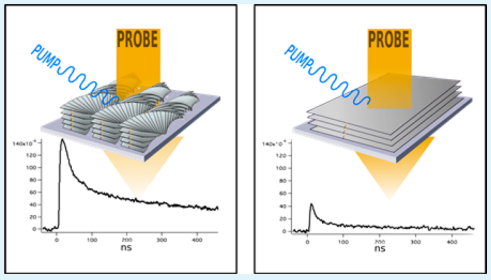

KEYWORDS: *helical nanofilaments, time-resolved microwave conductivity, bulk heterojunction, charge generation, liquid crystal*

INTRODUCTION

The helical nanofilament (HNF) phase[2,5] represents a promising self-assembling, nanosegregated architecture with potential as a good charge transporting system in an organic photovoltaic (OPV) system. A key potential advantage of the HNF phase involves the spontaneous formation of rigid twisted rods with nm metrics in two dimensions and the morphological control of liquid crystals in general (vide infra). As illustrated in Figure 1, molecules of HNF mesogens (in this case P-9-OPIMB, 1,3-phenylene bis[4-(4-nonyloxyphenyliminomethyl)-benzoate (Figure 1A)) self-assemble into twisted layers composed of aromatic and aliphatic sublayers (Figure 1B).

Within the aromatic sublayers, dynamic solid-state NMR data suggests the aromatic cores of the molecules are present in a "crystalline" environment, and electron diffraction experiments have revealed that the aromatic sublayers actually exist as crystalline "half-layers" in a rectangular lattice, with the "stretched" direction in aromatic half-layers oriented in nearly orthogonal directions.[4,25] Since the molecules in these half-layers are covalently bonded, the orthogonality of the rectangular lattices induces strain, which is relieved by negative Gaussian curvature of the layers, leading to a twisted layer structure as illustrated in Figure 1B. The degree of curvature in the twisted layers cannot be uniform and approaches zero as the layer width increases and as the number of layers in the stack (HNF thickness) increases.[1] This causes the width and thickness of the HNFs to spontaneously self-limit (~30 nm width, and ~5–8 layers per HNF) (Figure 1C). Thus, the twisted layers exist in stacks, with a small number of layers (5–8) in each stack, to form twisted HNFs (Figure 1C). The HNF length is unconstrained, and at the highest level of the hierarchical structure, the HNFs form a hexatic liquid crystalline supra-HNF self-assembly wherein the HNFs are parallel, and the twist is coherent (not shown). The HNF phase is polar, with the polar axis (shown in blue in Figures 1B,C), and macroscopic electric polarization, oriented along the HNF long axis. Half the surface area of the HNF is layer edges, in which the benzylidene aniline arm unit is in contact with the HNFs surroundings.

The HNF phase is necessarily porous and is robust to high levels of doping by small molecules, mesogens, and even polymers.[1−3] The Clark group has previously shown with XRD

Received: December 13, 2013
Accepted: March 3, 2014
Published: March 3, 2014

   dx.doi.org/10.1021/am405759d | ACS Appl. Mater. Interfaces 2014, 6, 4823−4830

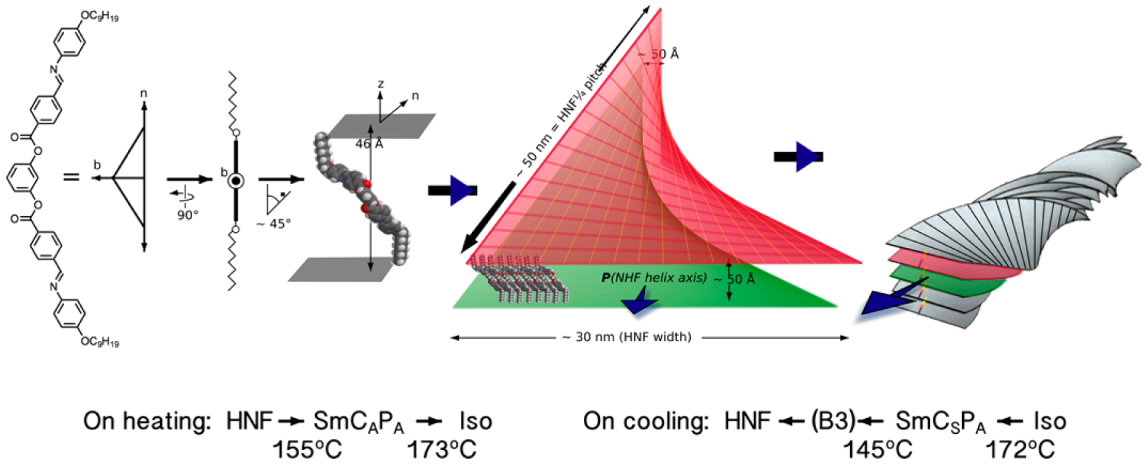

Figure 1. Hierarchical self-assembly of an HNF mesogen: A) the molecular structure of the HNF mesogen P-9-OPIMB with the transition temperatures and phase sequence observed on heating and cooling; B) illustration of the structure of a single twisted layer composed of HNF mesogens; C) stacking of the twisted layers produces "twisted rod"-shaped HNFs ~ 30 nm in diameter. The final stage of the self-assembly (not shown) involves liquid crystalline ordering of the HNFs into an hexatic phase where the HNF twist is coherent. The HNF bulk phase is necessarily porous, since twisted rods as illustrated in C cannot fill space.

and freeze-fracture TEM that the dopant molecules surround, but do not penetrate, individual nanofilaments.[3,4] This leads to a novel two-component composite with periodic nano-segregated domains of each component. It has been demonstrated that P-9-OPIMB forms HNFs when mixed with the soluble fullerene $PC_{60}BM$, though studies were limited to bulk mixtures.[2]

While detailed characterization of the bulk HNF phase has been reported,[1] understanding the structure of very thin films of the HNF phase, particularly in mixtures with other materials, is critical with regard to application in OPV. Herein, we report studies of thin films of the HNF mesogen P-9-OPIMB as neat thin films, bilayers with C_{60}, and as heterojunction mixtures with soluble fullerenes when prepared under different conditions.

The HNF phase can be grown with macroscopic orientation of the long axis of the rods through various methods, such as a thermal gradient, electric field, shearing, growing the phase from a nematic LC solvent, geometrical confinement, and cell surface properties controlled by self-assembled monolayers.[1,5−7] Macroscopic alignment would allow for the structuring of a device with the HNFs perpendicular to the substrate allowing for direct pathways to the electrodes.

A variety of mesogens have been found to form HNFs. Today, with only a few exceptions, all of the known HNF-forming mesogens contain a benzylideneaniline moiety.[8,9] The nature of the HNF mesogen "structure space" has not been adequately explored, and it is likely that HNF-forming mesogens with various different conjugated aromatic systems will be found.

Previous work on HNFs using the freeze-fracture transmission electron microscopy (FFTEM) technique have demonstrated that bulk HNF phase at a glass interface can exhibit toric and parabolic focal conic surface structures. These results illustrate the transition of the liquid crystal ordering between the glass substrate surface and the bulk HNFs.[10] The present study focuses on spin-cast thin films of P-9-OPIMB at an air interface and P-9-OPIMB-PCBM heterojunctions formed by these films. Strong surface effects are introduced by the large surface-to-volume ratio of the spin-cast thin films.

HNFs present a novel blended microstructure for potential use in OPV devices. They show promise as an active component of an OPV device due to the self-assembling formation of nanoscale aggregates with well-defined structure. The HNFs behave essentially as organic nanorods with diameter ~25−30 nm, approximately twice the typical exciton diffusion lengths found for many conjugated polymers, making a favorable environment for exciton diffusion to an electron donor - electron acceptor interface.[11,12] In addition, the smectic layers of the HNFs are crystalline, which has been correlated with enhanced carrier mobility and exciton diffusion in small molecule systems.[13,14] The nanofilaments can be aligned and have the potential to orient with their long axis normal to the electrodes, allowing direct charge transport to the layer ends, and to the electrodes for extraction.

Other self-assembling, liquid-crystalline systems have been explored for use in OPV.[15−17] One common approach is the use of columnar liquid crystal phases, which show promise with high carrier mobilities, from the large π-π overlap and alignability between electrodes.[18,19] However, columnar stacking promotes face to face packing of disk-shaped mesogens (discotics, such as phthalocyanine derivatives), thus limiting the orbital overlap of the mesogen and its electron acceptor, which can limit photoinduced charge transfer. In one recent study a 4.6% power conversion device was fabricated by phthalocyanine and C_{60} codeposition.[20]

In comparison to other self-assembling small molecule systems the HNFs have a particular advantage in that half of the surface area of the nanofilament is layer edges, which allow for contact between the P-9-OPIMB molecule and the electron acceptor. We postulate that this will lead to HNFs acting as an effective PET microstructure. In short, these properties of HNFs suggest they might be suitable materials for use in excitonic photovoltaics. This, to our knowledge, is the first work exploring this phase for use in donor−acceptor heterojunctions.[21]

It should be noted, however, that P-9-OPIMB is not an ideal material for OPV in most respects. The material represents a model for study of the effects of the heterojunction microstructure on photoinduced charge transfer. Specifically, the minimally conjugated benzilideneaniline arms of P-9-

OPIMB lead to a maximum absorption at 360 nm. Design of small bandgap mesogens based on HNF-forming mesogens will be necessary for their use in OPV devices. What is more, while HNFs have properties that may be advantageous in charge extraction, such as orientational alignment, this study is focused on morphological effects on photoinduced charge transfer.

In this work, TEM is employed to characterize the surface of spin-cast thin films and thus identify the liquid crystalline structuring, similar to its use in previous bulk studies of this HNF phase. These largely topographical data are complemented with XRD, which is used to probe liquid crystalline ordering throughout the sample. Together these techniques provide information on bulk order and microstructure in films of pure P-9-OPIMB as well as for the two-component samples.[22]

The electrodeless time-resolved microwave conductivity (TRMC) technique is used to probe the formation of mobile carriers in the heterojunction system, an indication of a donor–acceptor system that undergoes a photoinduced charge transfer. This allows photoconductivity characterization without fabrication of full photovoltaic devices and thus minimizes complications from electrodes and additional interfaces.

METHODS

Sample Preparation and Characterization. P-9-OPIMB was synthesized as previously described.[23] C_{60}, $PC_{60}BM$, $PC_{70}BM$, and bis-$PC_{60}BM$ were purchased from Nano-C Inc. Stock solutions of P-9-OPIMB and fullerenes were made in chloroform at concentrations of 10 g/L. Mixtures were made from relative volumes of stock solutions. Films were prepared by spin-coating solutions onto clean quartz substrates at 600 rpm for 60 s in a nitrogen-filled glovebox and then annealed on a hot plate for 5 min. Samples were placed on a preheated hot plate and then rapidly cooled by immediate placement from the hot plate to a room temperature metal surface. Bilayer films were made by depositing 30 nm of C_{60} with an Edwards thermal evaporator onto prepared P-9-OPIMB films. Samples were stored in the dark and measured in air.

TEM. Samples were cut from prepared quartz substrates and coated with 2 nm Pt at an angle of 45°, creating a shadowed replica of the samples surface. A 25 nm layer of carbon was then deposited as a support to the Pt replica. The sample was dissolved in ethyl acetate, and the replica floated and mounted on a Formvar-supported Cu TEM grid. The TEM images were taken with Phillips TEM. The angled deposition leads to a surface differentiation where dark areas are surfaces that face the deposition and light areas are shadowed from the deposition. Samples were measured to be between 100 and 350 nm thick as measured with a Tencor Instruments Alpha-step profilometer.

XRD. Diffraction measurements were taken on a Rigaku d/max diffractometer, with copper Kα radiation from a rotating anode set to 40 KV and 250 mA. $\theta/2\theta$ measurements were taken at a rate of 0.5°/minute. The diffractogram background was fit to a double-exponential decay and removed and the diffraction peaks fit to Gaussian curves. Instrument broadening was measured from Gaussian fit diffraction peak from LaB_6. The instrument broadening fwhm was determined to be 0.082° and was corrected with eq 1.

$$B_{\text{sample}} = \sqrt{B^2 - B_{\text{instrument}}^2} \tag{1}$$

Time-Resolved Microwave Conductivity. TRMC measurements were performed as described by Ferguson et al.[24] In short, samples were measured in an air-filled resonant microwave chamber (~8.9 GHz). A 4 ns laser pulse was generated from a Continuum Panther OPO pumped with a Nd:YAG laser source. Microwave loss was recorded with a Tektronix DPO 7254 oscilloscope for 450 ns after excitation at varying intensities of light. Signal was normalized by light absorption and irradiance. The inverse photocurrent plots at varying light intensities were fit to bi- and triexponential decays convoluted with an instrument response function and used to extrapolate the signal to $t = 0$.

The photoconduction is proportional to the change in the microwave power. The proportionality constant, K, is a measured value of the cavity resonance, as shown in eq 2. The photoconductivity, ΔG, is normalized by the absorbed light, I_0F_A, elementary charge, q_e, and a cavity dimension parameter, β, eq 3, resulting in a yield-mobility product.

$$\Delta G_{\text{exp}}(t) = -\frac{1}{K}\frac{\Delta P(t)}{P_o} \tag{2}$$

$$\phi(t)\Sigma\mu = \frac{\Delta G(t)}{\beta q_e I_0 F_A} \tag{3}$$

RESULTS AND DISCUSSION

TEM of Neat P-9-OPIMB Thin Films. Thin films of as-cast and annealed P-9-OPIMB are characterized with TEM to compare the well-studied bulk P-9-OPIMB microstructure with that of the thin films. Figure 2 shows the difference between as-cast and annealed films of P-9-OPIMB. In Figure 2A neat films of as-spun P-9-OPIMB present characteristics of the HNF phase. Specifically the repeating, twisted texture seen in Figure 2A has previously been identified as characteristic of the HNF phase.[1,10,25]

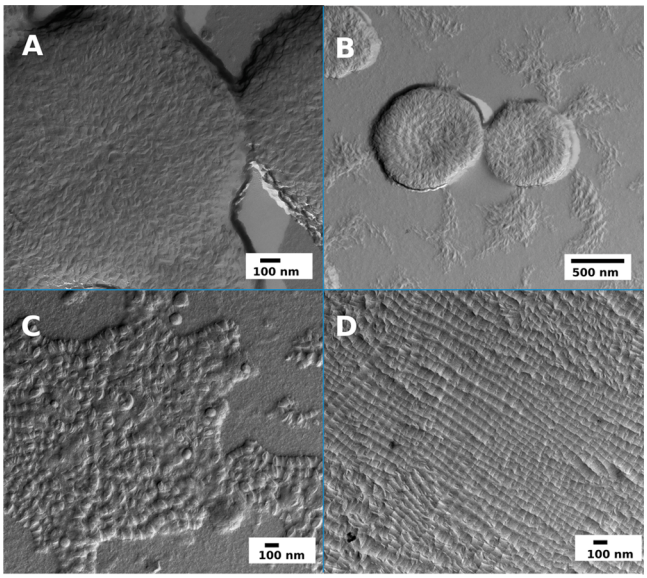

Figure 2. TEM images of as-spun and annealed P-9-OPIMB thin-films on quartz are presented. Images (A) and (B) are as-cast P-9-OPIMB films. Images (C) and (D) are thin films annealed to 165 °C. Dark areas in the TEM images arise from the incident angle of the Pt deposition.

The topology of the as-spun sample on the surface of the quartz is shown in Figure 2A. The P-9-OPIMB is dissolved in chloroform and spin-coated on the surface of the quartz. The rapid evaporation of chloroform causes the helical nanofilaments of P-9-OPIMB to quickly undergo nucleation and growth. During nucleation and subsequent rapid growth they form microdomains with helical nanofilaments radially pointing outward. More than 50% of the substrate area is covered by these domains, and helical nanofilaments are the dominant structure in the as-spun sample.

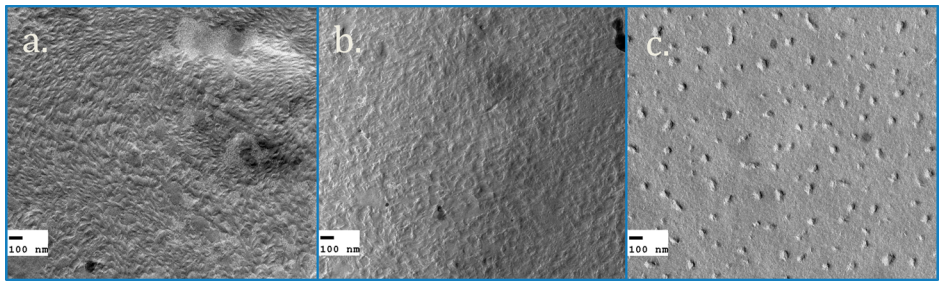

Figure 3. Thin films of P-9-OPIMB/$PC_{60}BM$ composites. Samples were annealed to different temperatures (A) 25 °C, (B) 150 °C, and (C) 240 °C.

Figure 2B shows HNF droplets on the substrate surface. This is a common feature in the as-spun films. The concentric circles in the droplets match the pitch of HNFs. The HNFs appear to nucleate and grow from the center outward.

The annealed sample, which is annealed to 165 °C between the HNF and SmC_AP_A phases, contains several surface structures, including the focal conics[10] and a small amount of HNFs. This is similar to the structures found at a glass interface from a broken planchet sample in work by Chen et al.[10] Because helical nanofilaments cannot make full contact with the surface, instead of forming helical nanofilaments, P-9-OPIMB form some typical lamellar surface structure. These regions are usually large. The P-9-OPIMB droplets present in the as-spun sample[10] are also observed but to a significantly smaller extent. The droplets merge upon annealing and no longer contain the orientation of the as-spun samples.

Spin-coating from a high vapor pressure solvent (chloroform) causes a macroscopically uneven surface, yet the well-ordered HNF texture is seen across most of the sample. Typically a thick film of P-9-OPIMB becomes better oriented and more regular upon annealing, yet these thin films do not. Thin annealed films of P-9-OPIMB form known, thermodynamically favored surface-driven microstructures, namely the parabolic focal conics shown in Figure 2C and 2D.

TEM of P-9-OPIMB/$PC_{60}BM$ Thin Films. Figure 3 shows 50% $PC_{60}BM$ in P-9-OPIMB composites processed under 3 different conditions, 1) as-spun, 2) annealed to 240 °C, above the clearing point of P-9-OPIMB, and 3) annealed to 150 °C, above the glass transition temperature but below the transition to the SmC_AP_A phase.

Akin to the behavior of as-spun films of P-9-OPIMB, as-spun mixtures of P-9-OPIMB and $PC_{60}BM$, Figure 3A, exhibit predominantly HNF textures. Several surface textures, like those in the annealed pure P-9-OPIMB films, are present in the films though only in a small portion of the sample; demonstrative TEM images are included in the Supporting Information along with descriptions. Mixed P-9-OPIMB-$PC_{60}BM$ films vary more than the neat P-9-OPIMB films. The mixed films do not contain the well-ordered droplets found with neat P-9-OPIMB samples. The samples include some larger droplets, but none similar to the symmetric, well-defined droplets in the neat as-spun samples. Despite the high levels of doping (50%$_{wt}$ $PC_{60}BM$) the composite films form HNF phases.

Figure 3C shows a film annealed above P-9-OPIMB's clearing point that demonstrates the tops of a lamellar texture, which appears flat. While the as-cast film varies between HNF and other textures (with a small portion of the images showing lamellar), the entire annealed composite sample is lamellar.

One unusual feature of the annealed films is the presence of the ~50 nm protrusions from the lamellar surface. These sparsely dispersed protrusions are clusters of $PC_{60}BM$, while all the other regions are the lamellar structure formed by P-9-OPIMB, as indicated by the layer steps. For comparison, an image showing clusters of $PC_{60}BM$ in the bulk helical nanofilament matrix is included in the Supporting Information. Similar features were seen in the bulk P-9-OPIMB-$PC_{60}BM$ mixtures by Chen et al. and identified as pockets of $PC_{60}BM$ crystallization.[2] Here we see the fullerene aggregates on the surface.

Images from sample 3, annealed to 150 °C, are exemplified in Figure 3b. These films are best described by considering a transition between the HNF phases seen in the as-prepared sample and the lamellar microstructure of the sample annealed above the clearing-point. This may be attributed to localized pockets of lamellar structure forming in the sample interspersed with areas of HNFs.

From the TEM data the as-cast films form the HNF phase upon rapid evaporation from the solvent. One-to-one by weight levels of doping with a soluble fullerene present HNF phase formation, further demonstrating the phase robustness. These films, when annealed in the presence of $PC_{60}BM$, transition to a surface-driven lamellar structure in which a large unquantified amount of $PC_{60}BM$ has migrated to the surface of the film.

XRD of Thin-Film Samples. Figure 4 shows X-ray diffractograms of as-spun and annealed P-9-OPIMB thin films, identically prepared to those measured with TEM,

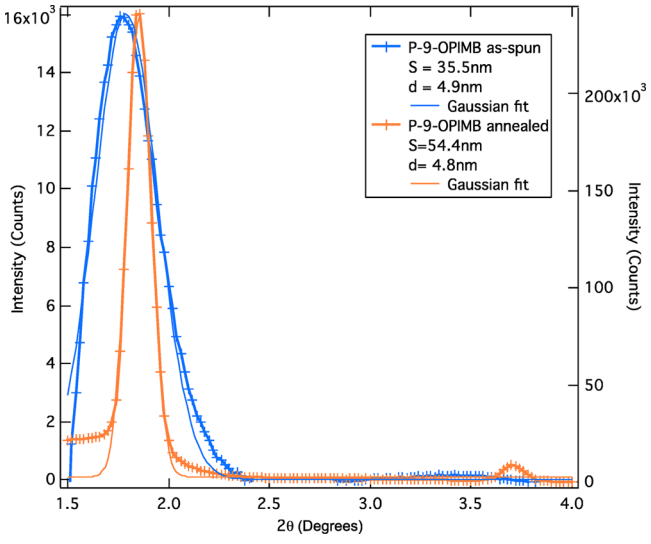

Figure 4. Diffractograms of as-spun and annealed (to 165 °C) thin films showing Bragg scattering from the layers are shown, along with their Gaussian fits. d is the smectic layer spacing. Only in the annealed P-9-OPIMB sample was a higher order diffraction peak detected.

annealed samples were heated at 165 °C. In both the as-cast and annealed samples a diffraction peak is found at approximately $2\theta = 1.8°$. The diffraction peak of the annealed sample is considerably sharper than that of the as-cast peak. The annealed sample also presents a second-order diffraction peak of 0.05× the peak height of the fundamental Bragg diffraction. Higher order peaks are more sensitive to the short-range disorder, in the as-cast film, the short-range disorder is greater, and thus no second-order peak is distinguishable.

The Gaussian-fit full-width at half-maximum (fwhm) is used to compare the correlation length of the smectic layers between samples. The correlation length increases as the number of continuous correlated smectic layers increases. The correlation length is inversely related to the peak widths. Thus, the HNF phase, where the number of correlated layers is limited to 5−8 layers due to the negative curvature, exhibits a broad peak, while annealing increases the correlation length of the layers leading to a sharper peak. The smectic layer spacing is determined by the peak diffraction angle, from eq 4.

$$d(\text{Å}) = \frac{\lambda}{2\sin\left(\frac{2\theta_{rad}}{2}\right)} \quad (4)$$

Helical nanofilaments have been previously characterized with XRD, with the primary identifying characteristic being the broad interlayer peak, arising from diffraction from the smectic layers near $2\theta = 1.8°$, and multiple intralayer peaks, arising from intermolecular diffraction within the smectic layers, near $2\theta = 21°$.[25] The quartz substrates lead to a significant background between 10° and 25°, which obscures intralayer diffraction as well as $PC_{60}BM$ crystallization peaks.[26]

The two samples show very similar layer spacing, calculated from the 2θ diffraction peak, indicating that the smectic layer spacing is largely unchanged when the sample is annealed. However the peak width varies greatly between as-spun and annealed samples, as can be seen in Figure 4. Here the fwhm is used to compare the as-spun and annealed peak width. The peaks were fit to a Gaussian and corrected from the instrument peak broadening as previously described. Some diffraction peaks are as sharp as the instrument limited standard (LaB_6) and are referred to as instrument limited.

A limited number of layers, typically between five and eight, are present in a single nanofilament formed by P-9-OPIMB. The as-spun sample, determined by TEM to consist of HNFs, has a fwhm of 0.200°. In the annealed sample the fwhm is instrument resolution limited, thus corresponding to a longer correlation length, over 100 nm (determined by the Scherrer equation, as demonstrated in the Supporting Information). HNFs have a set correlation length due to the limited smectic layer stacking growth, while a lamellar smectic phase is not similarly constrained. The sharper fwhm of the annealed sample indicates a longer correlation of smectic layers than would typically be found from the five to eight nanofilament layers. XRD evidence combines with thin film TEM images to confirm that the surface structures give a longer correlation length than HNFs and are easily identifiable by the relatively less difficult XRD technique.

Therefore the methodology is extended to other soluble fullerene and P-9-OPIMB samples, where fwhm and layer spacing, *d*, are shown in Table 1. Samples include different wt% mixtures of $PC_{60}BM$ and P-9-OPIMB in addition to 50% mixtures with two other common soluble fullerenes, bis-$PC_{60}BM$ and $PC_{70}BM$. In all cases the annealed-sample peak is measurably sharper than the as-spun (HNF) samples thus following the trend: annealing results in an HNF-to-lamellar transition.

Table 1. Comparison of As-Cast and Annealed Samples with Varying Concentrations of Soluble Fullerenes[a]

	as-cast		annealed (165 °C)	
$PC_{60}BM$ dopant	fwhm	d (nm)	fwhm	d (nm)
25% P-9-OPIMB	0.276	4.68	0.129	5.27
50% P-9-OPIMB	0.304	4.66	0.098	4.93
75% P-9-OPIMB	0.242	4.83	0 (RL)	4.62
100% P-9-OPIMB	0.200	4.94	0 (RL)	4.76
	as-cast		annealed (165 °C)	
50% P-9-OPIMB	fwhm	d (nm)	fwhm	d (nm)
$PC_{70}BM$	0.455	4.64	0.182	4.87
Bis-$PC_{60}BM$	0.236	4.86	0 (RL)	4.71

[a]FWHM correlation length is given along with the smectic layer spacing, *d*, for each sample. In each case the annealed sample also contained a small second-order diffraction peak. RL refers to an instrument resolution limited peak width.

Across the samples of increasing $PC_{60}BM$ loading the peak width of the annealed sample decreases. The as-spun films do not show a significant correlation between amount of fullerene doping and lamellar layer correlation length.

The smectic layer spacing does not consistently change as a result of the annealing. Some samples show an increase in layer spacing, whereas others show a decrease. The average change in peak spacing for the as-spun to annealed transition is 2.9 Å. This supports the hypothesis that the smectic layers and intermolecular structure of the phase remain nearly the same in the HNF-lamellar transition and that the HNF layers simply flatten to form smooth lamellar textures with more layers than are possible in the HNFs, without dramatically changing the internal structure of the layers.

XRD substantiates the TEM results that the as-spun P-9-OPIMB films form HNFs and upon annealing the mixed films change to either a lamellar or surface-driven microstructure depending on whether it is a neat mesogen or a fullerene composite, respectively. These "flattened" HNFs are strained due to the deformation from the preferred negative Gaussian curvature of the HNF layers, but interaction with a flat surface and the fullerene clustering apparently pays the energy cost of this strain.

Photoconductivity Studies on the P-9-OPIMB-C60 Bilayer. Photoinduced charge transfer between C_{60} and P-9-OPIMB helical nanofilaments is first evaluated in a bilayer and compared to a neat C_{60} film. Extending on the thin film characterization above, here we deposit a 30 nm layer of C_{60} onto a thin-film of helical nanofilaments. C_{60} deposition minimizes the influence of the electron acceptor on the solid-state microstructure such as that shown above when incorporating a soluble fullerene into the P-9-OPIMB structure. In both samples C_{60} is the sole absorbing species, and thus all excitons are generated in the C_{60} layer. It should be noted that the bilayer films are possibly not a true bilayer; the P-9-OPIMB thin film has a rough surface, and the C_{60} may penetrate into the layer. Thus the two components may have a larger surface area than that of an actual bilayer system.

Figure 5 compares the photoconductivity transient of a HNF-C_{60} bilayer (blue trace) and a pure C_{60} film (black trace) excited at 470 nm (6×10^{12} photons/cm^2.) The bilayer film is

dx.doi.org/10.1021/am405759d | ACS Appl. Mater. Interfaces 2014, 6, 4823−4830

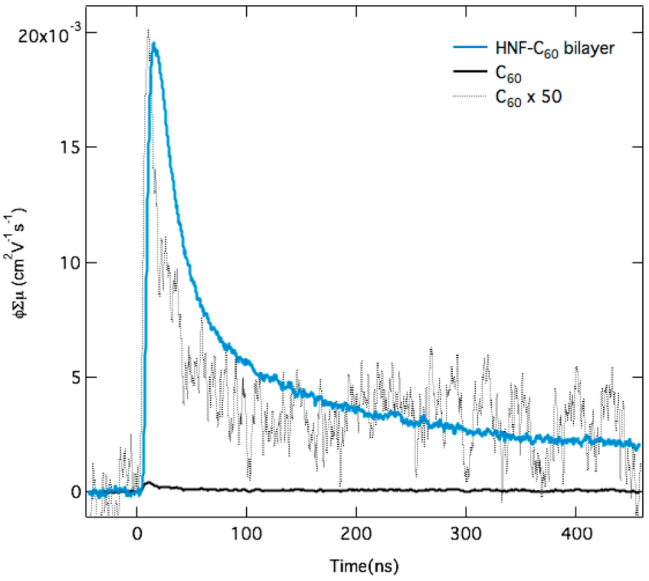

Figure 5. Yield-mobility product transients ($\Phi\Sigma\mu$) for films of pure C_{60} and bilayers of C_{60} on P-9-OPIMB nanofilaments.

composed of ~100 nm of P-9-OPIMB with a 30 nm layer of C_{60} compared to a 30 nm film of C_{60}. The photoconductivity of the bilayer film is 50 times larger than the pure C_{60} film.

The transient signal arises from a time-dependent photo-induced change in sample conductance. A direct relation of the microwave absorption can be made to the product of the number of charges in the system, ϕ, and their carrier mobility, μ, at ~8.9 GHz. The signal decays as charges recombine and encounter traps. Long-lived charges, such as those present at several hundred nanoseconds, are of particular interest to photovoltaic applications as the long-lived charges in a device are more likely to be extracted.

Photoconductance transients for the bilayer are evaluated by fitting the measured decays to a triexponential function, $F(t)$, eq 5 (convolved with an instrument response function.) The pure C_{60} film transients exhibit a single fast and slower decay and are more appropriately fit to a biexponential decay function. A maximum signal, $\Sigma_{i=1}^{3} A_i$, is obtained by extrapolating the decays to $t = 0$, a point in time that represents the largest number of photoinduced charges in the system.

$$F(t) = A_1 e^{-\frac{t}{\tau_1}} + A_2 e^{-\frac{t}{\tau_2}} + A_3 e^{-\frac{t}{\tau_3}} \quad (5)$$

The extrapolated $t = 0$ postpulse signal is large and is the maximum in the yield mobility product (eq 3). The large signal increase between the neat C_{60} and bilayer films suggests that the P-9-OPIMB helical nanofilaments are acting as a charge acceptor.

A sample consisting of 1 wt % $PC_{60}BM$ in P-9-OPIMB was measured to assess the microwave absorption contribution of P-9-OPIMB. It will be shown in the following section that $PC_{60}BM$ undergoes a photoinduced charge transfer with P-9-OPIMB, similar to C_{60}. $PC_{60}BM$ clustering is minimized with low wt% loading and thereby reduces the $PC_{60}BM$ electron contribution to the signal, as well as minimizing changes in the HNF microstructure.[27] The determined yield-mobility product value for a sample excited at 420 nm (only $PC_{60}BM$), $\phi_{t=0}\Sigma\mu = 4 \times 10^{-5}$ cm^2 V^{-1} s^{-1}, is therefore dominated by a contribution of only holes from the P-9-OPIMB (assuming a yield of 1 for the dispersed $PC_{60}BM$, gives us a lower limit on the hole-mobility in P-9-OPIMB of only $\sim 4 \times 10^{-5}$ cm^2 V^{-1} s^{-1}), which is significantly lower than the electron mobility in C_{60}, and it is valid to assume that only the latter contributes to the yield-mobility product. This allows for a direct comparison of the number of photogenerated charges (yield) in the pure C_{60} film and the HNF-C_{60} bilayer film.

The extrapolated $t = 0$ signal is measured and plotted for a variety of light fluences to account for light-dependent, charge-exciton annihilation as previously described by Ferguson et al.[24] This is observed as an increasing signal yield with decreasing light intensity. The double-logarithm plotted data is fit to the empirical modified-Dicker equation, eq 6,[28] plot and fit shown in the Supporting Information.[28−30] At the lower light intensities the signal asymptotically approaches A, where the carrier yield is proportional to the light intensity, and is similar to a solar fluence.

$$\phi_{t=0}\Sigma\mu = \frac{A}{1 + \sqrt{BI_0F_A + CI_0F_A}} \quad (6)$$

At low light intensity in the neat C_{60} film the measured mobility is the sum of the mobilities of the electrons and holes but is dominated by the former. We estimate the yield from the value of A, with the assumption that the total number of photogenerated holes and electrons in the C_{60} are equivalent, and the value of A is equal to the product of the yield of electrons and C_{60} electron mobility.

The lower-limit microwave mobility of the sum of the electron and hole charges in pure C_{60} was previously determined using pulse-radiolysis TRMC, $\Sigma\mu_{C60} = 0.29 \pm 0.07$ cm^2 V^{-1} s^{-1}.[31,32] Here we used the half PR-TRMC mobility to account for our observing only mobile electrons in C_{60}.

Assuming the C_{60} electron mobility dominates in both samples, a charge generation yield can be compared between the two samples. The pure C_{60} film has a charge-generation yield of <1%, whereas the HNF-C_{60} bilayer has a yield of 100% (with error margins of 25%). The charge-generation yield therefore appears to increase by 2 orders of magnitude between pure C_{60} and the bilayer. The photoinduced charge generation for the bilayer is high and can be attributed to efficient transfer of holes to the P-9-OPIMB in the HNFs.

Photoconductivity Studies on P-9-OPIMB-$PC_{60}BM$ Blends. As was determined from the TEM and XRD data, two distinct morphologies are created when mixing P-9-OPIMB and $PC_{60}BM$ and processing under different conditions. Here we compare those morphologies as bulk heterojunctions and probe charge-generation with TRMC.

Just as the comparison was made between the hole mobility in P-9-OPIMB and the electron mobility in C_{60}, electrons in the clustered or aggregated $PC_{60}BM$ phase have a far larger mobility than holes in P-9-OPIMB. Thus in the 50/50 heterojunction mixtures the microwave attenuation due to holes in P-9-OPIMB remains minimal, and the signal in these samples is dominated by electrons in the clustered $PC_{60}BM$.

Figure 6 shows the TRMC yield-mobility product signal for as-prepared HNF-$PC_{60}BM$ and annealed lamellar-$PC_{60}BM$ films as well as pure $PC_{60}BM$ films over a variety of light intensities. The HNF heterojunction shows nearly an order of magnitude larger signal than the lamellar sample. Additionally, the lamellar heterojunction transient has a very similar profile to that of pure $PC_{60}BM$. Modified Dicker A-values showed that at low light intensity the HNF-$PC_{60}BM$ sample (2.23×10^{-3}

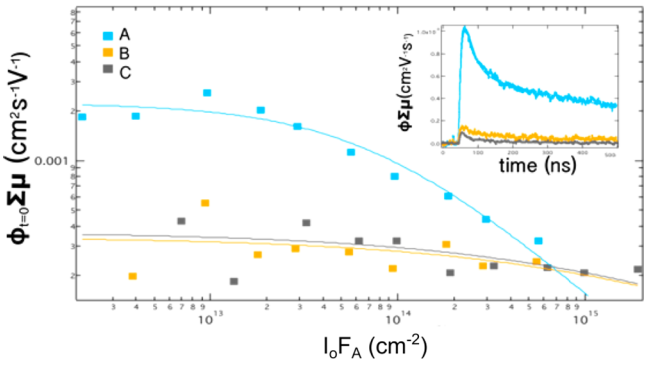

Figure 6. Yield-mobility plots of A) an as-prepared HNF-PCBM heterojunction, B) an annealed lamellar-PCBM heterojunction, and C) a pure PCBM film. The solid lines are fits to eq 6, as described in the text. Inset shows the absorption-normalized phototransients.

$cm^2\ V^{-1}\ s^{-1}$) has an order of magnitude larger signal than the lamellar sample (3.43×10^{-4} $cm^2\ V^{-1}\ s^{-1}$) and neat PCBM (3.67×10^{-4} $cm^2\ V^{-1}\ s^{-1}$). Yields can be extracted by using the PCBM electron mobility, as previously measured by PR-TRMC,[32] giving yields of 5.6% for HNF-PCBM and 0.9% for both the lamellar-PCBM and neat PCBM samples.

Akin to the charge generation results from the HNF-C_{60} bilayer the HNF heterojunction thin films confirms that HNFs act as a "good charge-generating interface". In addition to the increase in $t = 0$ signal, the HNF heterojunctions have much longer-lived charges with demonstrative half-life plots included in the Supporting Information.

The TEM images of the lamellar-$PC_{60}BM$ heterojunction show the presence of large ~50 nm $PC_{60}BM$ clusters. From the images it is unclear whether these clusters exist as droplets on the lamellar surface or spheres that penetrate into the lamellar layers. The lack of charge transfer that occurs between $PC_{60}BM$ and P-9-OPIMB in this system suggests that it may exist as the former. Photoinduced electron transfer (PET) may also be inhibited by the layer of P-9-OPIMB alkyl tails (an insulating layer between the excited $PC_{60}BM$ and the P-9-OPIMB at the heterojunction interface.) This is an issue important to the design of novel electron donor systems, such as small molecule, liquid-crystalline electron donors that rely on alkyl tails for liquid crystallinity or conductive polymers that frequently require alkyl tails for solubility.

The large increase in signal between the HNF-C_{60} bilayer and the pure C_{60} film show that the HNF phase is an effective bilayer interface for PET. What is more, this bilayer shows unity photoinduced change generation. This high yield was not observed in HNF-PCBM heterojunctions, but it is shown to increase the charge-generation in a heterojunction with $PC_{60}BM$ by an order of magnitude as compared to a lamellar packing of the same materials. The morphology has a significant impact on the resulting charge generation in the system, and the results should be used as a cautionary tail of soluble fullerenes' role affecting the liquid crystal phase of materials.

CONCLUSION

Thin films of P-9-OPIMB have been characterized. It is found that spin-casting films leads to the formation of helical nanofilaments (HNFs) but that the films transition to alternative curved surface-driven smectic structures upon annealing. The microstructure is also dependent on the presence of a fullerene dopant, which can trigger the formation of a lamellar surface-driven phase in which the fullerene macrophase separates as clusters on the surface of the flat liquid crystal layer.

High photoinduced charge transfer was seen in a bilayer of the HNF phase with C_{60}, showing that the HNF surface acted as a good interface for photoinduced electron transfer. This is attributed to the high degree of direct contact between the HNF layer edges, which contain the electron-donating benzylidene aniline aromatic units, and the C_{60} electron acceptor. We also compare PET in two P-9-OPIMB/$PC_{60}BM$ heterojunction systems, one which forms HNFs and the other transitions to a lamellar phase with large $PC_{60}BM$ clusters. Again the HNF is shown to be a good charge transfer microstructure. Moreover, the lamellar heterojunction structure causes no increase in photoconductivity over neat $PC_{60}BM$, showing that this microstructure inhibits electron transfer between the donor and acceptor. The lack of photoconductivity in these samples may be due to phase separation (clusters of PCBM were seen in the film replica TEM images), and it is of interest to the field of polymer and small molecule OPV to understand the role that PCBM may have in an annealed microstructure. Ultimately, the enhanced charge creation suggests the HNF phase has promising potential as a component of the heterojunction structure in OPV and warrants the design, synthesis, and characterization of energetically optimal mesogens that not only form the HNF phase but also can absorb light.

ASSOCIATED CONTENT

Supporting Information

Additional TEM images, information regarding XRD peak broadening, TRMC photoconductivity results and lifetime, and thin film absorption data. This material is available free of charge via the Internet at http://pubs.acs.org.

AUTHOR INFORMATION

Corresponding Author

*E-mail: walba@colorado.edu.

Notes

The authors declare no competing financial interest.

ACKNOWLEDGMENTS

This work was supported by the National Science Foundation Graduate Research Fellowship award no. DGE-1144083 as well as the National Science Foundation Materials Research Science and Engineering Center, award no. DMR-0820579. The authors would like to acknowledge and thank Alex Nardes and Art Klittnick for profilometry measurements and Nikos Kopidakis and Hilary Marsh for insightful discussions. The TRMC system described here was funded by the Solar Photochemistry Program, Division of Chemical Sciences, Geosciences, and Biosciences, Office of Basic Energy Sciences, U.S. Department of Energy under Contract No. DE-AC36-08-GO28308 with the National Renewable Energy Laboratory.

REFERENCES

(1) Chen, D.; Maclennan, J.; Shao, R.; Yoon, D.; Wang, H.; Korblova, E.; Walba, D.; Glaser, M.; Clark, N. Chirality-Preserving Growth of Helical Filaments in the B4 Phase of Bent-Core Liquid Crystals. *J. Am. Chem. Soc.* **2011**, *133*, 12656−12663.

(2) Chen, D.; Zhu, C.; Wang, H.; Maclennan, J.; Glaser, M.; Korblova, E.; Walba, D.; Rego, J.; Soto-Bustamante, E.; Clark, N.

Nanoconfinement of Guest Materials by Helical Nanofilament Networks of Bent-Core Mesogens. *Soft Matter* **2013**, *9*, 462−471.
(3) Zhu, C.; Chen, D.; Shen, Y.; Jones, C.; Glaser, M.; Maclennan, J.; Clark, N. Nanophase Segregation in Binary Mixtures of a Bent-Core and a Rodlike Liquid-Crystal Molecule. *Phys. Rev. E* **2010**, *81*, 011704.
(4) Chen, D.; Zhu, C.; Shoemaker, R.; Korblova, E.; Walba, D.; Glaser, M.; Maclennan, J.; Clark, N. Pretransitional Orientational Ordering of a Calamitic Liquid Crystal by Helical Nanofilaments of a Bent-Core Mesogen. *Langmuir* **2010**, *26*, 15541−15545.
(5) Kim, H.; Lee, S.; Shin, T.; Cha, Y.; Korblova, E.; Walba, D.; Clark, N.; Lee, S.; Yoon, D. Alignment of Helical Nanofilaments on the Surfaces of Various Self-Assembled Monolayers. *Soft Matter* **2013**, *9*, 6185−6191.
(6) Yoon, D.; Yi, Y.; Shen, Y.; Korblova, E.; Walba, D.; Smalyukh, I.; Clark, N. Orientation of a Helical Nanofilament (B4) Liquid-Crystal Phase: Topographic Control of Confinement, Shear Flow, and Temperature Gradients. *Adv. Mater.* **2011**, *23*, 1962−1967.
(7) Araoka, F.; Sugiyama, G.; Ishikawa, K.; Takezoe, H. Highly Ordered Helical Nanofilament Assembly Aligned by a Nematic Director Field. *Adv. Funct. Mater.* **2013**, *23*, 2701−2707.
(8) Tsai, E.; Richardson, J.; Korblova, E.; Nakata, M.; Chen, D.; Shen, Y.; Shao, R.; Clark, N.; Walba, D. A Modulated Helical Nanofilament Phase. *Angew. Chem., Int. Ed.* **2013**, *52*, 5254−5257.
(9) Bialecka-Florjanczyk, E.; Sledzinska, I.; Gorecka, E.; Przedmojski, J. Odd-Even Effect in Biphenyl-Based Symmetrical Dimers with Methylene Spacer - Evidence of the B4 Phase. *Liq. Cryst.* **2008**, *35*, 401−406.
(10) Chen, D.; Heberling, M.; Nakata, M.; Hough, L.; Maclennan, J.; Glaser, M.; Korblova, E.; Walba, D.; Watanabe, J.; Clark, N. Structure of the B4 Liquid Crystal Phase Near a Glass Surface. *ChemPhysChem* **2012**, *13*, 155−159.
(11) Kim, J.; Kim, K.; Ko, S.; Kim, W. Optimum Design of Ordered Bulk Heterojunction Organic Photovoltaics. *Sol. Energy Mater. Sol. Cells* **2011**, *95*, 3021−3024.
(12) Clarke, T.; Durrant, J. Charge Photogeneration in Organic Solar Cells. *Chem. Rev.* **2010**, *110*, 6736−6767.
(13) Najafov, H.; Lee, B.; Zhou, Q.; Feldman, L.; Podzorov, V. Observation of Long-Range Exciton Diffusion in Highly Ordered Organic Semiconductors. *Nat. Mater.* **2010**, *9*, 938−943.
(14) Lunt, R.; Benziger, J.; Forrest, S. Relationship Between Crystalline Order and Exciton Diffusion Length in Molecular Organic Semiconductors. *Adv. Mater.* **2010**, *22*, 1233−1236.
(15) Ohno, A.; Haruyama, A.; Kurotaki, K.; Hanna, J. Charge-Carrier Transport in Smectic Mesophases of Biphenyls. *J. Appl. Phys.* **2007**, *102*, 083711.
(16) Iino, H.; Ohno, A.; Hanna, J. Hole Mobility and Lifetime in a Smectic Liquid Crystalline Photoconductor of a 2-Phenylnaphthalene Derivative. *J. Chem. Phys.* **2005**, *123*, 244701.
(17) Wu, J.; Usui, T.; Hanna, J. Synthesis of a Novel Smectic Liquid Crystalline Glass and Characterization of its Charge Carrier Transport Properties. *J. Mater. Chem.* **2011**, *21*, 8045−8051.
(18) Eccher, J.; Faria, G.; Bock, H.; von Seggern, H.; Bechtold, I. Order Induced Charge Carrier Mobility Enhancement in Columnar Liquid Crystal Diodes. *ACS Appl. Mater. Interfaces* **2013**, *5*, 11935−11943.
(19) Hayashi, H.; Nihashi, W.; Umeyama, T.; Matano, Y.; Seki, S.; Shimizu, Y.; Imahori, H. Segregated Donor-Acceptor Columns in Liquid Crystals That Exhibit Highly Efficient Ambipolar Charge Transport. *J. Am. Chem. Soc.* **2011**, *133*, 10736−10739.
(20) Meiss, J.; Merten, A.; Hein, M.; Schuenemann, C.; Schafer, S.; Tietze, M.; Uhrich, C.; Pfeiffer, M.; Leo, K.; Riede, M. Fluorinated Zinc Phthalocyanine as Donor for Efficient Vacuum-Deposited Organic Solar Cells. *Adv. Funct. Mater.* **2012**, *22*, 405−414.
(21) Olson, D.; Lee, Y.; White, M.; Kopidakis, N.; Shaheen, S.; Ginley, D.; Voigt, J.; Hsu, J. Effect of Polymer Processing on the Performance of Poly(3-hexylthiophene)/ZnO Nanorod Photovoltaic Devices. *J. Phys. Chem. C* **2007**, *111*, 16640−16645.
(22) Pisula, W.; Zorn, M.; Chang, J.; Mullen, K.; Zentel, R. Liquid Crystalline Ordering and Charge Transport in Semiconducting Materials. *Macromol. Rapid Commun.* **2009**, *30*, 1179−1202.
(23) Akutagawa, T.; Matsunaga, Y.; Yasuhara, K. Mesomorphic Behavior of 1,3-Phenylene Bis[4-(4-alkoxyphenylimonomethyl)-benzoates] and Related-Compounds. *Liq. Cryst.* **1994**, *17*, 659−666.
(24) Ferguson, A.; Kopidakis, N.; Shaheen, S.; Rumbles, G. Quenching of Excitons by Holes in Poly(3-hexylthiophene) Films. *J. Phys. Chem. C* **2008**, *112*, 9865−9871.
(25) Hough, L.; Jung, H.; Kruerke, D.; Heberling, M.; Nakata, M.; Jones, C.; Chen, D.; Link, D.; Zasadzinski, J.; Heppke, G.; Rabe, J.; Stocker, W.; Korblova, E.; Walba, D.; Glaser, M.; Clark, N. Helical Nanofilament Phases. *Science* **2009**, *325*, 456−460.
(26) Mens, R.; Chambon, S.; Bertho, S.; Reggers, G.; Ruttens, B.; D'Haen, J.; Manca, J.; Carleer, R.; Vanderzande, D.; Adriaensens, P. Description of the Nanostructured Morphology of [6,6]-Phenyl-C-61-butyric Acid Methyl Ester (PCBM) by XRD, DSC and Solid-State NMR. *Magn. Reson. Chem.* **2011**, *49*, 242−247.
(27) Coffey, D.; Larson, B.; Hains, A.; Whitaker, J.; Kopidakis, N.; Boltalina, O.; Strauss, S.; Rumbles, G. An Optimal Driving Force for Converting Excitons into Free Carriers in Excitonic Solar Cells. *J. Phys. Chem. C* **2012**, *116*, 8916−8923.
(28) Dicker, G.; de Haas, M.; Siebbeles, L.; Warman, J. Electrodeless Time-Resolved Microwave Conductivity Study of Charge-Carrier Photogeneration in Regioregular Poly(3-hexylthiophene) Thin Films. *Phys. Rev. B* **2004**, *70*, 045203.
(29) Dayal, S.; Kopidakis, N.; Rumbles, G. Photoinduced Electron Transfer in Composites of Conjugated Polymers and Dendrimers with Branched Colloidal Nanoparticles. *Faraday Discuss.* **2012**, *155*, 323−337.
(30) Reid, O.; Malik, J.; Latini, G.; Dayal, S.; Kopidakis, N.; Silva, C.; Stingelin, N.; Rumbles, G. The Influence of Solid-State Microstructure on the Origin and Yield of Long-Lived Photogenerated Charge in Neat Semiconducting Polymers. *J. Polym. Sci., Part B: Polym. Phys.* **2012**, *50*, 27−37.
(31) Hoofman, R.; vanderLaan, G.; deHaas, M.; Tanigaki, K. Charge Migration in Pulse-Irradiated Undoped C60 Powder Studied with the Time-Resolved Microwave Conductivity Technique. *Synth. Met.* **1997**, *86*, 2355−2356.
(32) de Haas, M.; Warman, J.; Anthopoulos, T.; de Leeuw, D. The Mobility and Decay Kinetics of Charge Carriers in Pulse-Ionized Microcrystalline PCBM Powder. *Adv. Funct. Mater.* **2006**, *16*, 2274−2280.